J. Fluid Mech. (2014), *vol.* 755, *pp.* 603–627. © Cambridge University Press 2014
doi:10.1017/jfm.2014.439

Evolution of localized disturbances in the elliptic instability

Yuji Hattori[1,†] **and Mohd Syafiq bin Marzuki**[1]

[1]Institute of Fluid Science, Tohoku University, Sendai 980-8577, Japan

(Received 7 October 2013; revised 22 April 2014; accepted 25 July 2014;
first published online 22 August 2014)

The time evolution of localized disturbances in an elliptical flow confined in an elliptical cylinder is studied by direct numerical simulation (DNS). The base flow is subject to the elliptic instability. The unstable growth of localized disturbances predicted by the short-wavelength stability analysis is captured. The time evolution can be divided into four stages: linear, weakly nonlinear, nonlinear and turbulent. In the linear stage a single wavepacket grows exponentially without changing its shape. The exponential growth is accompanied by large oscillations which have time period half that of the fluid particles in the elliptical flow. An averaged wavepacket, which is a train of bending waves that has a finite spatial extent, also grows exponentially, while the oscillations of the growth rate are small. The averaged growth rate increases as the kinematic viscosity decreases; the inviscid limit is close to the value predicted by the short-wavelength stability analysis. In the weakly nonlinear stage the energy stops growing. The vortical structure of the initial disturbances is deformed into wavy patterns. The energy spectrum loses the peak at the initial wavenumber, developing a broad spectrum, and the flow goes into the next stage. In the nonlinear stage weak vorticity is scattered in the whole domain although strong vorticity is still localized. The probability density functions (p.d.f.) of a velocity component and its longitudinal derivative are similar to those of isotropic turbulence; however, the energy spectrum does not have an inertial range showing the Kolmogorov spectrum. Finally in the turbulent stage fine-scale structures appear in the vorticity field. The p.d.f. of the longitudinal derivative of velocity shows the strong intermittency known for isotropic turbulence. The energy spectrum attains an inertial range showing the Kolmogorov spectrum. The turbulence is not symmetric because of rotation and strain; the component of vorticity in the compressing direction is smaller than the other two components. The energy of the mean flow as well as the total energy decreases. The ratio of the lost energy to the initial energy of the mean flow is large in the core region.

Key words: parametric instability, transition to turbulence, vortex flows

1. Introduction

It is well known that a strained vortex is subject to a parametric instability known as the elliptic instability. Vortices appearing in a wide variety of phenomena and

† Email address for correspondence: hattori@fmail.ifs.tohoku.ac.jp

https://doi.org/10.1017/jfm.2014.439 Published online by Cambridge University Press

engineering applications are often immersed in straining flows which are the most fundamental two-dimensional perturbations. For example, wingtip vortices behind an aircraft, whose persistence prohibits frequent traffic in airports, induce straining flows mutually so that they are subject to the elliptic instability. Thus it is important to understand the characteristic features of the elliptic instability and its physical mechanism.

There have been a number of studies on the elliptic instability (Kerswell 2002). Moore & Saffman (1975) and Tsai & Widnall (1976) first showed analytically that a line vortex in a strain field is unstable to three-dimensional disturbances; the instability occurs as a consequence of parametric resonance of two neutrally stable inertial waves under strain. Pierrehumbert (1986) found that localized modes centred at an elliptic stagnation point have exponential growth rate which is independent of the wavelength in the short-wave limit. Inspired by his work Bayly (1986) considered an elliptical flow that extends infinitely and Fourier modes with time-dependent wavevectors as disturbances, which had been used in rapid distortion theory (Moffatt 1967; Godeferd, Cambon & Leblanc 2001); it is a simple model which allows us to obtain analytical solutions without difficulties. Bayly (1986) revealed the essential mechanism of the elliptic instability: it is the growing Floquet mode with the resonance angle of the wavevector being $\pi/3$. His work was followed by Waleffe (1989, 1990) who gave a physical interpretation: the vorticity stays in the stretching direction and this leads to an exponential growth. Waleffe (1989) also considered the elliptic instability in a bounded domain using modal stability analysis; the linear growth rate is obtained analytically in the inviscid limit and saturation of the instability and a feedback to the mean flow are discussed using a weakly nonlinear analysis; see Gledzer & Ponomarev (1992) for linear stability results in an elliptical cylinder.

The analytical results have been confirmed by experiments (Malkus 1989; Leweke & Williamson 1998; Eloy, Le Gal & Le Dizès 2000; Meunier & Leweke 2005). They have also been confirmed by numerical simulations, which can also pursue the nonlinear evolution. Mason & Kerswell (1999) considered the elliptic instability in an elliptical cylinder taking account of viscous effects; after confirming the linear instability results they showed numerically that weakly nonlinear saturation, which is predicted by amplitude equations, cannot be observed. Lundgren & Mansour (1996) studied the stability and transition to turbulence of flattened two-dimensional Taylor–Green vortices subjected to the elliptic instability by direct numerical simulation (DNS); although the resolution was low, with 256^3 modes, the energy spectrum was shown to have a range proportional to the Kolmogorov spectrum in the turbulent stage. Laporte & Corjon (2000) and Le Dizès & Laporte (2002) performed DNS and large-eddy simulations of the elliptic instability in a counter-rotating vortex pair; the stages leading to transition to turbulence were clarified. Faddy & Pullin (2005) considered an array of counter-rotating vortices that have axial flow; they found not only cooperative elliptic instabilities but also that strong axial flow leads to modes with significantly higher growth rates. Schaeffer & Le Dizès (2010) analysed the nonlinear dynamics of the elliptic instability both in a strained vortex and in two counter-rotating vortices; shear layer formation and vortex loop ejection were shown to occur in the nonlinear transition. However, most of these numerical studies use low-wavenumber disturbances like bending waves in order to trigger the elliptic instability. In addition they are limited to the moderate Reynolds numbers of less than 10^4 which are encountered in the laboratory experiments, although the Reynolds number can be much larger for wingtip vortices and other important applications.

The analysis of the elliptic instability has been mostly done by the normal-mode stability analysis, in which the disturbance is decomposed into eigenmodes

https://doi.org/10.1017/jfm.2014.439 Published online by Cambridge University Press

(Moore & Saffman 1975; Tsai & Widnall 1976; Eloy & Le Dizès 2001; Fukumoto 2003). One of the important features of the elliptic instability is that it is a short-wave instability; the inviscid growth rate does not vanish in the short-wave limit. Thus short-wavelength stability analysis (Friedlander & Vishik 1991; Lifschitz & Hameiri 1991) has been another effective tool for analysing the elliptic instability. In short-wavelength stability analysis the disturbance is assumed to be a wavepacket whose wavelength is small; the linearized Euler equation is reduced to a set of ordinary differential equations which is solved analytically or numerically with much less effort. Bayly (1986) and Waleffe (1990) can be regarded as using short-wavelength stability analyses since the smooth flow in the neighbourhood of any elliptic stagnation point is approximated by elliptical flow and these analyses are valid for short-wavelength disturbances; see also Godeferd *et al.* (2001) for the relation between the short-wavelength stability analysis and that of Bayly (1986) and Waleffe (1990). Although limited to the short-wave limit it elucidates physical mechanisms (Waleffe 1990) which are sometimes obscured in the normal-mode analysis. It gives the correct limit of the growth rate obtained by the normal-mode analysis, as shown for the elliptic instability (Le Dizès & Eloy 1999; Eloy & Le Dizès 2001; Fukumoto 2003) as well as for the curvature instability (Hattori & Fukumoto 2003; Fukumoto & Hattori 2005; Hattori & Fukumoto 2009, 2010, 2012, 2014), which is another parametric instability of vortices induced by the curvature of the vortex tubes.

To the authors' knowledge, however, the results obtained by the short-wavelength stability analysis have not been identified or reproduced directly in experiments or in numerical simulations. In fact it is difficult to capture the unstable solutions predicted by the short-wavelength stability analysis since the short-wave disturbances are damped by viscous effects; the Reynolds number should be high, which requires high computational cost to capture them. In this context recent works by Shukhman (2007) and Cohen *et al.* (2010) which studied localized vortex evolution in planar homogeneous flows, including the elliptical flow, in an attempt to interpret the generation of hairpin vortices in shear flows are worth noting.

We should point out that there are remarkable differences in the stability properties due to boundary conditions. In unbounded elliptical flow the single Fourier-mode solutions considered by Bayly (1986) and Waleffe (1990) are exact solutions of the full nonlinear Euler equations so that the unstable solutions grow linearly forever; nonlinear effects do not enter this problem. For strained vortices with finite cores the boundary conditions together with the vorticity distribution specify the structures of eigenmodes and nonlinearity plays a crucial role when the amplitude of the disturbances becomes large. There is a difference between strained vortices in an unbounded domain (Leweke & Williamson 1998; Laporte & Corjon 2000; Le Dizès & Laporte 2002; Faddy & Pullin 2005; Meunier & Leweke 2005; Schaeffer & Le Dizès 2010) and elliptical flow bounded by a wall (Malkus 1989; Waleffe 1989; Gledzer & Ponomarev 1992; Mason & Kerswell 1999; Eloy *et al.* 2000): the Crow instability (Crow 1970), which is a long-wave instability, exists for strained vortices in an unbodied domain but is absent from elliptical flow bounded by a wall in which isolated branches of inertial waves disappear.

In this paper we study the evolution of localized disturbances which are wavepackets of short wavelengths in the elliptic instability by DNS to reveal the linear and nonlinear stability properties. As a first step toward exploring the properties of strained vortices that have general vorticity distribution we choose the elliptical flow confined in an elliptical cylinder as a base flow. We show that a localized disturbance in the form of a wavepacket does grow exponentially, keeping the initial structure as

https://doi.org/10.1017/jfm.2014.439 Published online by Cambridge University Press

predicted by the short-wavelength stability analysis, which assumes the flow to be inviscid and in the short-wave limit, even when both the Reynolds number and the wavenumber of the disturbance are high but finite. After confirming linear stability properties the nonlinear process leading to turbulence is investigated.

There is also a practical reason why localized disturbances are important. It is easier to introduce localized disturbances, whose energy is small in general because of small spatial extent, than normal modes, which extend periodically. Thus they can be used to control strained vortices by destabilization. In doing so we should understand not only the linear but also the nonlinear stability properties. In the linear stage the evolution of a localized disturbance can be expanded by the eigenmodes in principle (Arendt, Fritts & Andreassen 1997). However, it is not always easy to reconstruct its evolution and understand its behaviour from the expansion since the eigenmodes are not mutually orthogonal in general; even in the case of elliptical flow bounded by a wall where orthogonality holds, reconstruction is not always an effective method for studying the evolution of localized disturbances.

This paper is organized as follows. In § 2 we describe the problem and the numerical method. In § 3 we first give an overview of the time evolution of localized disturbances; after showing that the time evolution can be decomposed into four stages, each stage is investigated in detail. Finally we conclude in § 4.

2. Formulation

2.1. *Base flow*

We consider the time evolution of a localized disturbance in an elliptical flow inside an elliptical cylinder. We choose a Cartesian coordinate system in which the velocity and vorticity fields of the elliptical flow are given by

$$\boldsymbol{u}_0 = (-y + \epsilon x)\boldsymbol{e}_x + (x - \epsilon y)\boldsymbol{e}_y, \quad \boldsymbol{\omega}_0 = 2\boldsymbol{e}_z, \tag{2.1a,b}$$

respectively, where ϵ is the rate of strain which is uniform and $\boldsymbol{e}_x$, $\boldsymbol{e}_y$ and $\boldsymbol{e}_z$ are unit vectors along the x, y and z directions, respectively. The elliptical flow is an exact solution of the incompressible Navier–Stokes equations. As shown in figure 1 the major and minor axes of the elliptic streamlines lie on $y = x$ and $y = -x$, respectively. We prefer these tilted axes although a natural choice would be the x and y axes. There are two reasons for this: (i) it is possible to accommodate a larger elliptic flow in a square domain; (ii) the principal axes of the strain coincide with the x, y and z axes as the strain tensor is

$$\boldsymbol{S}_0 = \left(\frac{1}{2}\left(\frac{\partial u_i}{\partial x_j} + \frac{\partial u_j}{\partial x_i}\right)\right) = \begin{pmatrix} \epsilon & 0 & 0 \\ 0 & \epsilon & 0 \\ 0 & 0 & 0 \end{pmatrix}. \tag{2.2}$$

The surface of the cylinder moves with the same velocity as the elliptical flow so that the no-slip condition is satisfied. This flow is approximately realized in the experiments by Malkus (1989) and Eloy *et al.* (2000). The total energy of the flow can increase since the flow is driven at the boundary.

2.2. *Disturbance*

We decompose the flow $\boldsymbol{u}$ into the sum of the base flow and a disturbance: $\boldsymbol{u} = \boldsymbol{u}_0 + \boldsymbol{u}'$. In the short-wavelength stability analysis the time evolution of an

https://doi.org/10.1017/jfm.2014.439 Published online by Cambridge University Press

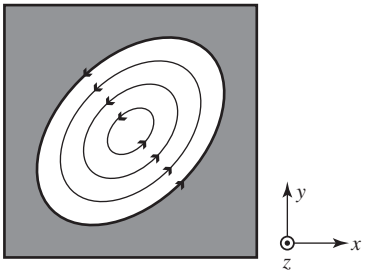


FIGURE 1. Elliptical flow inside an elliptical cylinder immersed in a periodic box.

infinitesimal disturbance in the form of a wavepacket $\boldsymbol{u}' = \exp[\mathrm{i}\Phi(\boldsymbol{x}, t)/\delta](\boldsymbol{a} + O(\delta))$ is governed by

$$\frac{\mathrm{d}\boldsymbol{X}}{\mathrm{d}t} = \boldsymbol{u}_0(\boldsymbol{X}), \quad \frac{\mathrm{d}\boldsymbol{k}}{\mathrm{d}t} = -\boldsymbol{L}^{\mathrm{T}}\boldsymbol{k}, \quad \frac{\mathrm{d}\boldsymbol{a}}{\mathrm{d}t} = \left(\frac{2\boldsymbol{k}\boldsymbol{k}^{\mathrm{T}}}{|\boldsymbol{k}|^2} - \boldsymbol{I}\right)\boldsymbol{L}\boldsymbol{a}, \tag{2.3a–c}$$

where $\boldsymbol{X}$ is the particle motion and $L_{ij} = \partial u_{0,i}/\partial x_j$ (Friedlander & Vishik 1991; Lifschitz & Hameiri 1991). This set of equations is derived from the linearized Euler equation by expanding in powers of δ which is assumed small; $\boldsymbol{k} = \nabla\Phi(\boldsymbol{X}(t), t)$ and $\boldsymbol{a}$ denote the local wavevector and the amplitude, respectively. The incompressibility condition is satisfied if $\boldsymbol{k}\cdot\boldsymbol{a} = 0$ at $t = 0$.

In the present study the localized disturbance is a wavepacket of finite spatial extent centred at the origin. We consider two types. One is a single wavepacket given by

$$\boldsymbol{u}' = \nabla \times \boldsymbol{A}, \quad \boldsymbol{A} = \beta_0 \boldsymbol{A}_0 \exp\left(-|\boldsymbol{x}|^2/r_0^2\right)\cos\left(\boldsymbol{k}_0\cdot\boldsymbol{x}\right), \quad \boldsymbol{k}_0 = k_0\,[\sin\chi, 0, \cos\chi]^{\mathrm{T}}, \tag{2.4}$$

where r_0 and β_0 determine the spatial extent and the amplitude of the disturbance, respectively; note that the vector potential $\boldsymbol{A}$ for $\boldsymbol{u}'$ is used in the above equation to ensure the incompressibility condition. The vectors $\boldsymbol{A}_0$ and $\boldsymbol{k}_0$ are chosen by taking account of the results obtained by the short-wavelength stability analysis. For example, the initial condition of the unstable disturbance at resonance is given by $\chi = \pi/3$ and $\boldsymbol{A}_0 = [1/2, 0, -\sqrt{3}/2]^{\mathrm{T}}$ (Bayly 1986; Waleffe 1990).

The single wavepacket defined above rotates without significant change of its shape when $\epsilon = 0$. The other type of localized disturbance is the average of the single wavepacket over one period of motion; the vector potential is

$$\boldsymbol{A} = \beta_s \exp\left(-|\boldsymbol{x}|^2/r_0^2\right)\sum_{j=1}^{N}\boldsymbol{A}_j\cos(\boldsymbol{k}_j\cdot\boldsymbol{x}), \tag{2.5}$$

where

$$\boldsymbol{k}_j = k_0[\cos\phi_j\sin\chi, \sin\phi_j\sin\chi, \cos\chi]^{\mathrm{T}}, \quad \phi_j = \frac{2\pi j}{N}. \tag{2.6}$$

The initial condition of the unstable solution is given by $\chi = \pi/3$; the vector potential is obtained by solving (2.3):

$$\boldsymbol{A}_j = \left[7/8 - (3/8)\cos 2\phi_j, -(3/8)\sin 2\phi_j, -\sqrt{3}/2\cos\phi_j\right]^{\mathrm{T}} \tag{2.7}$$

(Bayly 1986; Waleffe 1990). The initial conditions of the single wavepacket and the averaged wavepacket are shown in figure 2.

https://doi.org/10.1017/jfm.2014.439 Published online by Cambridge University Press

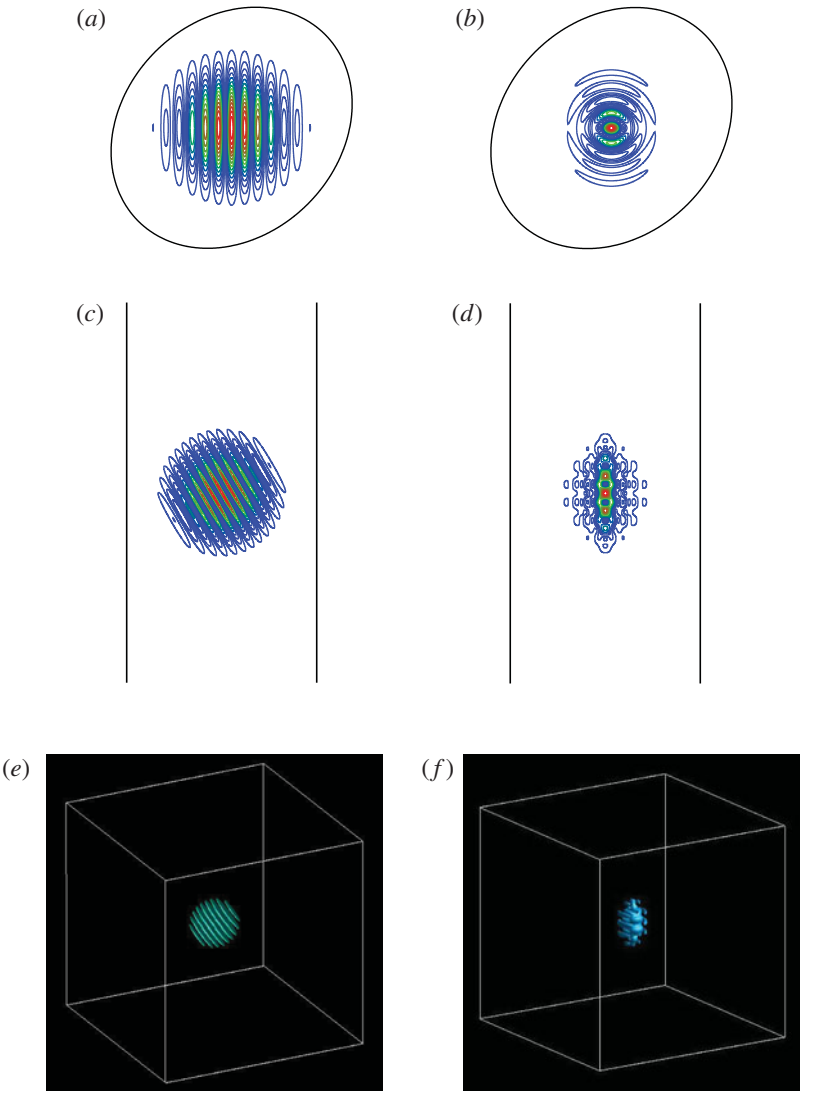


FIGURE 2. Initial disturbance. Contours of the magnitude of vorticity $|\boldsymbol{\omega}_d|$ on $z = 0$ (a,b) and $y = 0$ (c,d); iso-surface of $|\boldsymbol{\omega}_d|$ (e,f): (a,c,e) single wavepacket; (b,d,f) averaged wavepacket.The contour levels are $(1/16)\omega_{max}$ (blue line), $(2/16)\omega_{max}$, ..., $(16/16)\omega_{max}$ (red line), ω_{max} being the instantaneous maximum of $|\boldsymbol{\omega}_d|$ on $z = 0$ or $y = 0$. The value of $|\boldsymbol{\omega}_d|$ of the iso-surface is $0.25\omega_{max}$ (e) and $0.2\omega_{max}$ (f) ω_{max} being the maximum of $|\boldsymbol{\omega}_d|$ in the domain.

2.3. *Numerical method*

A high-precision method is required in the present study since we intend to capture both the time evolution of a localized disturbance that has small amplitude initially and the final turbulent state that includes a wide range of scales. One way to simulate such a flow in the elliptical cylinder is to employ the non-orthogonal elliptico-polar coordinate system used in Mason & Kerswell (1999). Although it is suitable for imposing the boundary conditions at the surface of the cylinder, a severe condition

https://doi.org/10.1017/jfm.2014.439 Published online by Cambridge University Press

for the time step must be satisfied as the grid size near the z axis becomes very small. Thus we use the volume penalization method (Arquis & Caltagirone 1984; Angot, Bruneau & Fabrie 1999), which is now established as a successful immersed boundary method and has been applied to DNS of turbulent flows (Schneider & Farge 2005). In this method we solve the three-dimensional incompressible Navier–Stokes equations supplemented by penalization terms

$$\frac{\partial \boldsymbol{u}}{\partial t} + \boldsymbol{u}\cdot\nabla\boldsymbol{u} = -\frac{1}{\rho_0}\nabla p + \nu\nabla^2\boldsymbol{u} - \frac{\Xi}{\eta}(\boldsymbol{u}-\boldsymbol{u}_b), \tag{2.8}$$

$$\nabla\cdot\boldsymbol{u} = 0, \tag{2.9}$$

where ρ_0 is the uniform density, ν is the kinematic viscosity, η is the permeability which is small, and $\boldsymbol{u}_b$ is the velocity inside the cylinder. Here the mask function Ξ defined by

$$\Xi(\boldsymbol{x}) = \begin{cases} 0 & \text{if } \boldsymbol{x} \text{ is inside the elliptical cylinder,} \\ 1 & \text{otherwise} \end{cases} \tag{2.10}$$

differentiates the fluid region and the rigid body. The velocity field $\boldsymbol{u}_b$ coincides with that of the elliptical flow in the neighbourhood of the surface of the cylinder so that the no-slip boundary conditions are satisfied; it decays to zero at the boundary of the box to ensure periodic boundary conditions.

The Fourier pseudo-spectral method is used for spatial discretization. The aliasing errors are removed by a combination of phase shift and truncation. The fourth-order Runge–Kutta method is used for the temporal evolution.

2.4. *Decomposition of the flow field*

The total velocity field is decomposed into the mean field $\boldsymbol{u}_m$ and the disturbance fields $\boldsymbol{u}_d$ as

$$\boldsymbol{u} = \boldsymbol{u}_m + \boldsymbol{u}_d, \quad \boldsymbol{u}_m = \sum_{\boldsymbol{k},k_z=0} \tilde{\boldsymbol{u}}_{\boldsymbol{k}} \mathrm{e}^{\mathrm{i}\boldsymbol{k}\cdot\boldsymbol{x}}, \quad \boldsymbol{u}_d = \sum_{\boldsymbol{k},k_z\neq 0} \tilde{\boldsymbol{u}}_{\boldsymbol{k}} \mathrm{e}^{\mathrm{i}\boldsymbol{k}\cdot\boldsymbol{x}}, \tag{2.11}$$

where $\tilde{\boldsymbol{u}}_{\boldsymbol{k}}$ is the Fourier coefficient of the velocity field. This simple and efficient method of decomposition is used instead of extracting the elliptical flow, which would be an appropriate method, because the results shown below do not differ significantly from those obtained by the latter method. In fact there is no discernible difference between them in the linear stage; the difference becomes large with the amplitude of the disturbance in the other stages as the mean flow is modified. However, the picture obtained below does not differ much if the method of decomposition is changed since the difference between the base and mean flow energy is roughly proportional to the energy of the disturbance.

In the next section we show the energy spectrum of the disturbance, which is defined as

$$E(k) = \sum_{\|\boldsymbol{k}|-k|<\Delta k/2} |\tilde{\boldsymbol{u}}_{\boldsymbol{k}}|^2, \tag{2.12}$$

where $\Delta k = 1$. We should be careful in interpreting the energy spectrum since the disturbance is confined in the elliptical cylinder while the Fourier transform is performed in the periodic box. In other words we are dealing with functions filtered by $1-\Xi$ which have jumps at the surface of the cylinder. This filtering may produce a spurious spectrum proportional to k^{-2} at high wavenumbers when the disturbance is

https://doi.org/10.1017/jfm.2014.439 Published online by Cambridge University Press

distributed in the whole fluid region. Thus the spectrum at high wavenumbers should be interpreted carefully. However, the $k^{-5/3}$ spectrum in the turbulent stage shown in the next section is not an artifact since the spurious spectrum is steeper than the $k^{-5/3}$ spectrum so that the latter dominates at high wavenumbers. The effects of the jumps on the energy spectrum are detailed in appendix A.

2.5. *Simulation parameters*

The strain rate is set to $\epsilon = 0.2$, which is of the same order of magnitude as $\epsilon \approx 0.1$ in the experiment by Eloy *et al.* (2000) and can be regarded small. The elliptical cylinder

$$x^2 + y^2 - 2\epsilon xy = \left(\frac{\pi}{2}\right)^2, \tag{2.13}$$

whose major and minor axes are $\pi/(1-\epsilon)^{1/2}$ and $\pi/(1+\epsilon)^{1/2}$, respectively, is immersed in a periodic box $[-\pi, \pi]^3$. The ratio of the volume of the fluid region to that of the periodic box is approximately 20 %, which may be regarded small; this value cannot be increased very much, however, since the rigid body part should be thick enough for $\boldsymbol{u}_b$ to decay smoothly from the elliptical flow at the surface of the cylinder to zero at the boundary of the box. The number of Fourier modes is 512^3, while the range of effective wavenumbers is $|k_i| \leqslant 241 \approx (\sqrt{2}/3)512$. The spatial resolution is sufficiently fine to capture the small scale of turbulence as $k_{max}\eta \approx 1.17$, where η_K is the Kolmogorov scale, is large enough (Ishihara *et al.* 2007); see also appendix B for accuracy of the numerical simulation.

The parameter values of the initial disturbance are specified as follows. The wavenumber is fixed to $k_0 = 20$. The angle χ is usually set to the resonance angle $\chi = \pi/3$, although $\chi = \pi/4$ and $5\pi/12$ are also tested to see what happens for off-resonance conditions. The parameter r_0 which determines the spatial extent of the disturbance is $r_0 = \pi/5$. The amplitudes β_0 and β_s are chosen so that the ratio of the energy of the initial disturbance to that of the elliptical flow is 1.57×10^{-8}.

The kinematic viscosity is $5 \times 10^{-5} \leqslant \nu \leqslant 2 \times 10^{-4}$, which implies that the Reynolds number based on the total circulation of the elliptical flow is $1.23 \times 10^4 \leqslant Re_\Gamma = \Gamma/\nu \leqslant 4.93 \times 10^4$. The permeability is set to $\eta = 10^{-3}$ after checking that the results do not change significantly by lowering the value to $\eta = 2 \times 10^{-4}$. The time step is $\Delta t = 10^{-3}$.

3. Results

3.1. *Overview of the time evolution of localized disturbances*

Figure 3 shows the time evolution of the energy E, instantaneous growth rate σ and average of the squared wavenumber $\overline{k^2}$ of the disturbance, which are defined as

$$E = \int_V |\boldsymbol{u}_d|^2 \, \mathrm{d}V, \quad \sigma = \frac{1}{E}\frac{\mathrm{d}E}{\mathrm{d}t}, \quad \overline{k^2} = \frac{\displaystyle\sum_{\boldsymbol{k},k_z\neq 0} k^2 |\tilde{\boldsymbol{u}}_{\boldsymbol{k}}|^2}{\displaystyle\sum_{\boldsymbol{k},k_z\neq 0} |\tilde{\boldsymbol{u}}_{\boldsymbol{k}}|^2}, \tag{3.1a–c}$$

where V is the flow region. This figure suggests that the time evolution of localized disturbances can be divided into four stages: the linear, weakly nonlinear, nonlinear and turbulent stages. In the linear stage ($0 \leqslant t \lesssim 90$ in the single wavepacket case; $0 \leqslant$

https://doi.org/10.1017/jfm.2014.439 Published online by Cambridge University Press

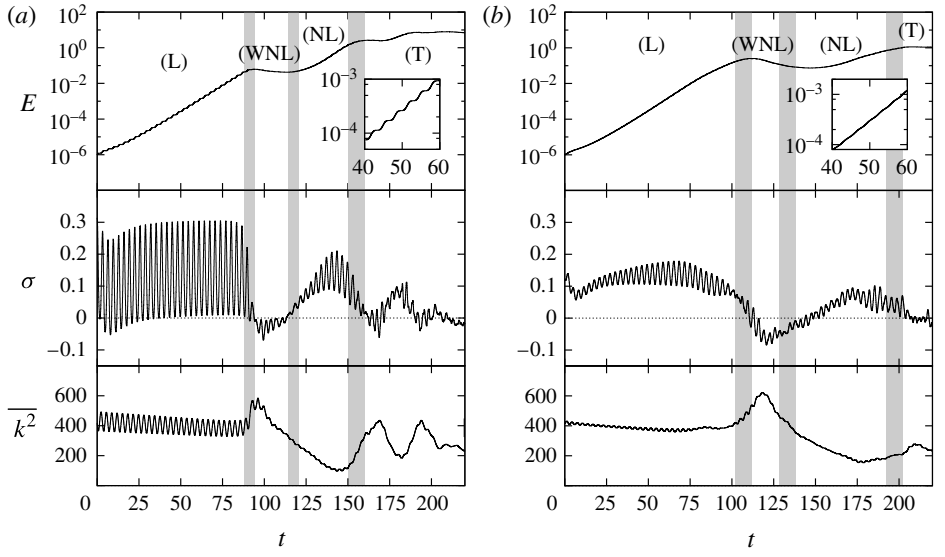


FIGURE 3. Time evolution of energy (top), instantaneous growth rate (middle) and average of squared wavenumber (bottom) of the disturbance: (*a*) single wavepacket, (*b*) averaged wavepacket. The grey bars divide the time evolution into four stages: linear (L), weakly nonlinear (WNL), nonlinear (NL) and turbulent (T). $\nu = 10^{-4}$.

$t \lesssim 110$ in the averaged wavepacket case, and so on) the energy grows exponentially on average, while the instantaneous growth rate oscillates with a large amplitude for the single wavepacket; $\overline{k^2}$ fluctuates around the initial value $k_0^2 = 400$. In the weakly nonlinear stage ($90 \lesssim t \lesssim 120$; $110 \lesssim t \lesssim 130$) the growth of the energy saturates; $\overline{k^2}$ increases for a while and then decreases. In the nonlinear stage ($120 \lesssim t \lesssim 150$; $130 \lesssim t \lesssim 190$) the energy grows exponentially again, while $\overline{k^2}$ decreases further. Finally the flow becomes fully turbulent ($150 \lesssim t$; $190 \lesssim t$).

Figure 4 shows what happens if the angle χ of the wavevector is different from the resonance angle $\pi/3$. For $\chi = \pi/4$ and $5\pi/12$ the energy of the disturbance decreases on average until $t \approx 25$. After $t \approx 25$, however, it starts growing exponentially with growth rates comparable with the resonant case $\chi = \pi/3$. This is because the initial wavepacket involves a small fraction of the resonant unstable wavepacket.

In the following we investigate the characteristic features of each stage.

3.2. *Linear stage*

As we have already seen in figure 3, the energy of the disturbance grows exponentially with large oscillations for the single wavepacket. The time period of the oscillations is close to half that of fluid particle motion in elliptical flow $T \approx 2\pi$. This is because the fluid particles in elliptical flow twice pass both the x axis, which is the stretching direction, and the y axis, which is the compressing direction, in one period of rotation. Figure 5 compares the growth rate of the energy and enstrophy of the disturbances, the latter being defined as

$$\sigma_\Omega = \frac{1}{\Omega}\frac{\mathrm{d}\Omega}{\mathrm{d}t}, \quad \Omega = \int_V |\boldsymbol{\omega}_d|^2 \, \mathrm{d}V, \quad \boldsymbol{\omega}_d = \boldsymbol{\nabla} \times \boldsymbol{u}_d. \tag{3.2}$$

Clearly the time evolution of the two growth rates are nearly in anti-phase.

https://doi.org/10.1017/jfm.2014.439 Published online by Cambridge University Press

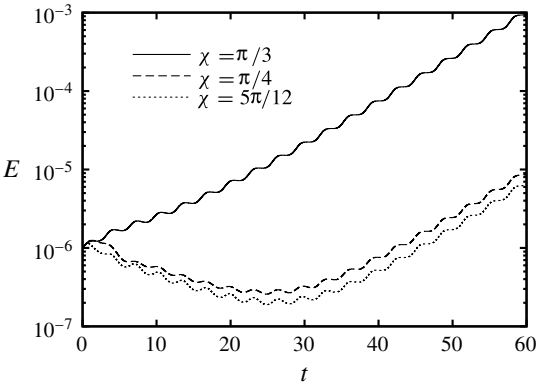


FIGURE 4. Effect of the angle χ of the wavenumber vector on the time evolution of energy of the disturbance. Single wavepacket. $\nu = 10^{-4}$.

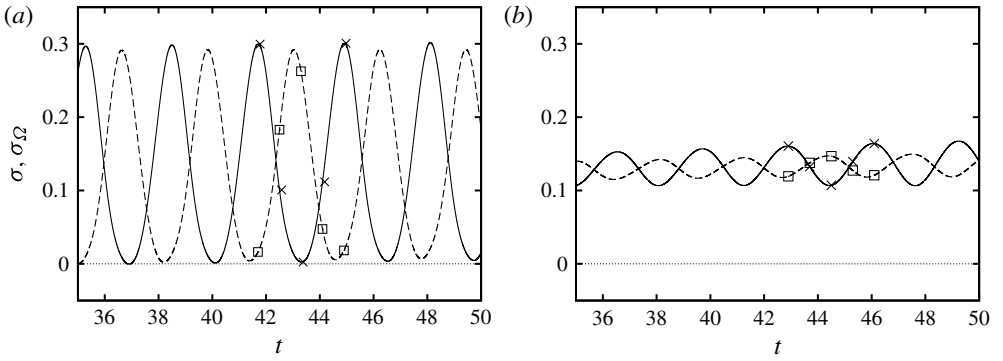


FIGURE 5. Instantaneous growth rate of energy (solid lines) and enstrophy (dashed lines) of the disturbance for $35 \leqslant t \leqslant 50$. The symbols correspond to the instants chosen in figures 6 and 8. $\nu = 10^{-4}$. (*a*) Single wavepacket, (*b*) averaged wavepacket.

The time evolution of the disturbances in time $T/2$ is shown by contours of $|\boldsymbol{\omega}_d|$ in figure 6. The five instants are marked by symbols in figure 5. In the single-wavepacket case the disturbance rotates with the elliptical flow, keeping the initial structure of the wavepacket with a little deformation; the disturbance is elongated in the z direction compared to the initial condition. The growth rate of enstrophy σ_Ω takes its local minima at $t = 41.7$ and 44.9; at these instants the wavevector is along the x axis in the xy plane so that $\boldsymbol{\omega}_d$, which is perpendicular to the wavevector, avoids the x axis or stretching direction and is along the z axis. This is confirmed in figure 7 which shows that the ratio Ω_x/Ω of the x component in the enstrophy is minimum and that of the z component Ω_z/Ω is maximum, where

$$\Omega_\alpha = \int_V \omega_\alpha^2 \mathrm{d}V, \quad \alpha = x, y, z. \tag{3.3}$$

Conversely σ_Ω reaches its local maximum at $t = 43.3$ when the wavevector is along the y axis in the xy plane; correspondingly $\boldsymbol{\omega}_d$ is along the stretching direction as $\Omega_x/\Omega \approx 1$ (figure 7). Note that Ω_y/Ω is close to zero throughout the linear stage,

https://doi.org/10.1017/jfm.2014.439 Published online by Cambridge University Press

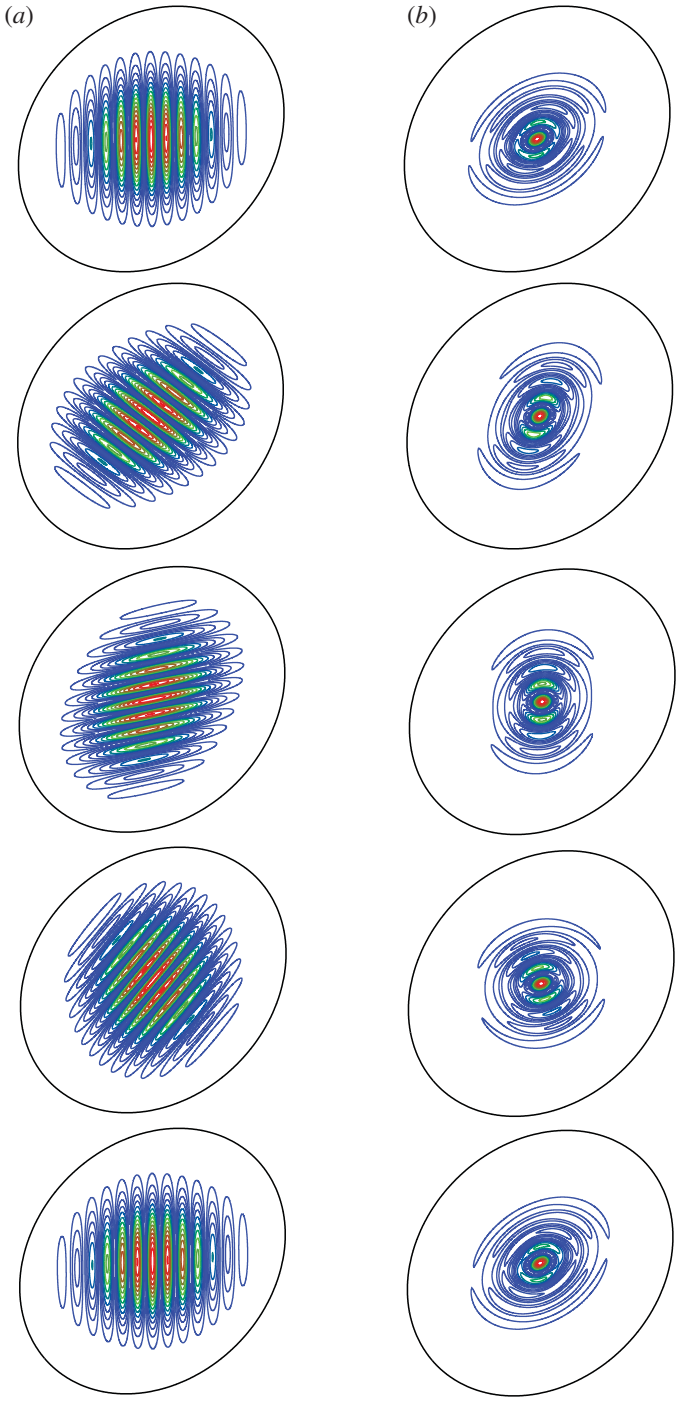


FIGURE 6. Time evolution of the disturbance in a half-period of rotation of the elliptical flow. Contours of the magnitude of vorticity $|\boldsymbol{\omega}_d|$ on $z = 0$. The contour levels are the same as in figure 2. $\nu = 10^{-4}$. (*a*) Single wavepacket, $t = 41.7, 42.5, 43.3, 44.1, 44.9$ (from the top to the bottom); (*b*) averaged wavepacket, $t = 42.9, 43.7, 44.5, 45.3, 46.1$.

https://doi.org/10.1017/jfm.2014.439 Published online by Cambridge University Press

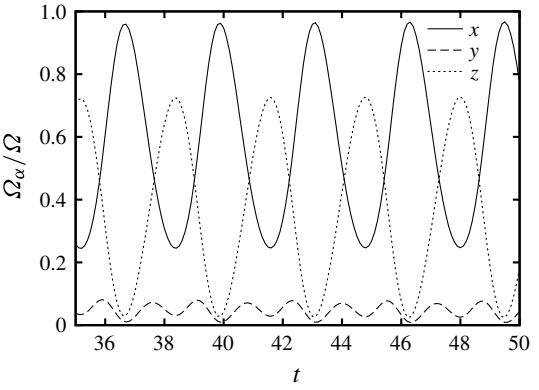


FIGURE 7. Time evolution of the component ratio of enstrophy. Single wavepacket. $\nu = 10^{-4}$.

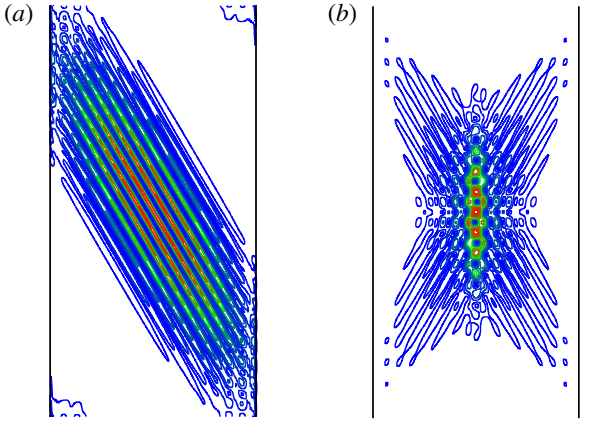


FIGURE 8. Structure of the disturbance at the latest instant of figure 6. Contours of the magnitude of vorticity $|\boldsymbol{\omega}_d|$ on $y = 0$. The contour levels the are same as in figure 2. $\nu = 10^{-4}$. (*a*) single wavepacket, $t = 44.9$; (*b*) averaged wavepacket, $t = 46.1$.

which implies that the unstable disturbance avoids the compressing direction. The contours of $|\boldsymbol{\omega}_d|$ on $y = 0$ at $t = 44.9$ clearly show that the angle between the wavevector and the z axis does not vary from $\chi = \pi/3$, supporting that the initial structure of the wavepacket is maintained (figure 8).

In the averaged-wavepacket case the contours near the centre or origin are ellipses which do not deform very much as time proceeds although the outer contours rotate with the elliptical flow (figure 6). As shown in figure 8 the disturbance is a train of bending waves which bends in the stretching direction. However, in contrast to the bending waves obtained by modal stability analysis, which usually have large amplitudes near the boundary and are spatially periodic along the z axis, the disturbance is localized near the z axis and has a finite extent along it.

The averaged growth rate is shown as a function of kinematic viscosity in figure 9 for the single wavepacket. The growth rate is averaged in a time interval where the growth rate is nearly periodic. It decreases monotonically with kinematic viscosity which dissipates the energy of the disturbances. Also shown in the figure by the dotted

https://doi.org/10.1017/jfm.2014.439 Published online by Cambridge University Press

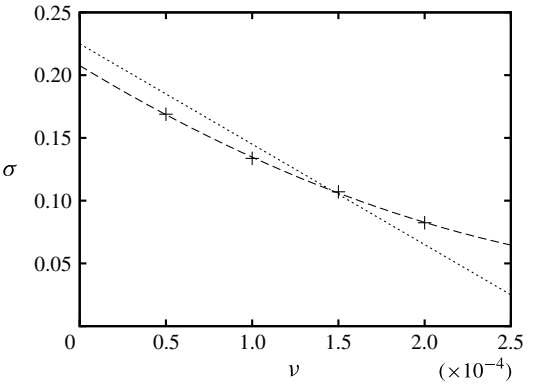


FIGURE 9. Averaged growth rate as a function of viscosity. Symbols: numerical results; dashed line: approximation curve of the numerical results; dotted line: prediction (3.4). Single wavepacket.

line is a simple prediction of the growth rate in the limit of small strain

$$\sigma = \sigma_{SW} - 2\nu k_0^2, \quad \sigma_{SW} = 2\epsilon\left(\tfrac{9}{16}\right) = 0.225, \tag{3.4}$$

where σ_{SW} is the growth rate obtained in the short-wave limit (Waleffe 1990) and $-2\nu k_0^2$ is the viscous damping of the Fourier modes (Landman & Saffman 1987). The numerical results are slightly smaller than (3.4) for small ν, while they are slightly larger than (3.4) for large ν. There are several reasons for these differences: the strain is not as small; the wavenumber is finite; and the disturbance does not consist of a single Fourier mode as observed in the energy spectrum (figure 10*a*). Although the energy spectrum peak at $k = k_0$ grows exponentially as time proceeds, its shape changes slowly as the modes that are initially small grow rapidly.

3.3. *Weakly nonlinear stage*

Hereafter we focus on the single-wavepacket case. In the weakly nonlinear stage the energy of the disturbance stops growing (figure 3). This saturation is often predicted by weakly nonlinear analysis which also predicts the subsequent decay. In the present case, however, the energy decays only slightly and then the flow goes into the nonlinear stage, which agrees with Mason & Kerswell (1999) who showed that in the case of low-wavenumber modes the duration of the weakly nonlinear state is short because of a secondary instability. The average of the squared wavenumber $\overline{k^2}$ increases early in the weakly nonlinear stage since harmonics of the wavepacket are excited. Then it decreases as low-wavenumber modes grow (figure 10*b*). Finally the peak at $k = k_0$ of the energy spectrum is lost.

The structure of the disturbance in the weakly nonlinear stage is shown in figure 11(*a*,*b*). Although it is different from the structure of the wavepacket in the linear stage, strong vorticity exists in wavy structures that are reminiscent of the wavepacket. It is most likely that the deformation of the wavepacket into wavy patterns is caused by an interaction of the packet with its envelope whose size $r_c = \pi/5$ corresponds to wavenumber $k \approx 10$ which is comparable with the wavenumber of the undulation of strong vorticity. The disturbance is still localized as the probability density function (p.d.f.) of the velocity component w differs from a Gaussian distribution, in contrast to the nonlinear and turbulent stages (figure 12).

https://doi.org/10.1017/jfm.2014.439 Published online by Cambridge University Press

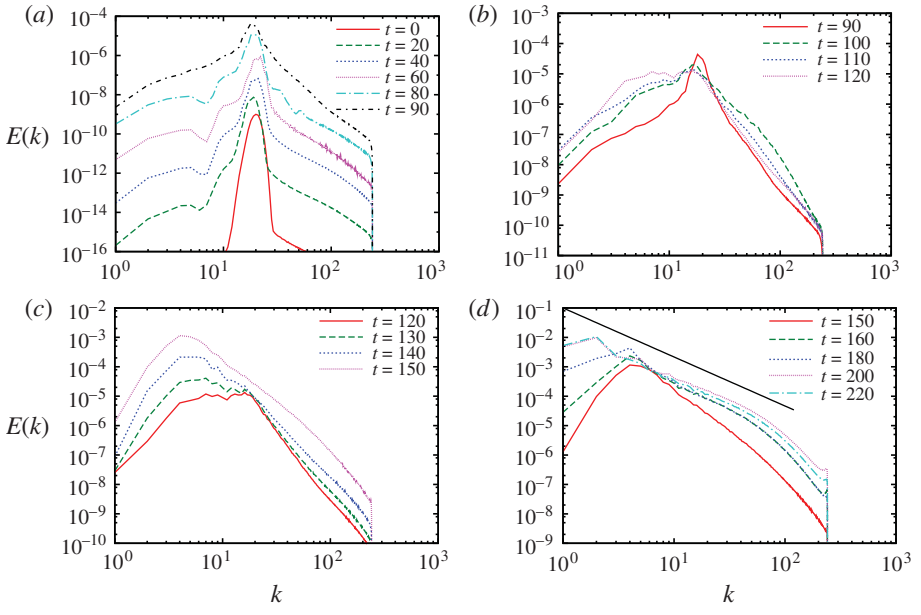


FIGURE 10. (Colour online) Energy spectrum of the disturbance. Single wavepacket. $\nu = 10^{-4}$. (*a*) Linear stage, (*b*) weakly nonlinear stage, (*c*) nonlinear stage, (*d*) turbulent stage. The solid line in (*d*) is proportional to $k^{-5/3}$.

3.4. *Nonlinear stage*

In the nonlinear stage the energy of the disturbance grows exponentially again (figure 3). Although strong vorticity is still localized, weak vorticity is now scattered in the whole domain (figure 11*c*,*d*). As a result the p.d.f. of the velocity component w is close to a Gaussian distribution except for large $|w|$, while that of $\partial u/\partial x$ shows intermittency (figure 12). However, the flow is not fully turbulent; the energy spectrum broadens, but it does not have a $k^{-5/3}$ spectrum (figure 10*c*). In addition, unlike fully developed turbulence the second-order structure function has no range approximately proportional to $r^{2/3}$ (figure 13).

3.5. *Transition to turbulence*

Transition to turbulence occurs in $140 \lesssim t \lesssim 160$, which is about three rotations of the elliptical flow, as shown below. Figure 15 shows the time evolution of the component ratio Ω_α/Ω ($\alpha = x, y, z$) of the enstrophy and the skewness of $\partial u/\partial x$ in the time interval $100 \leqslant t \leqslant 200$. The component ratio comes close to $1/3$ that corresponds to equipartition of energy, but never reaches it as the final turbulent state has asymmetry due to strain; in fact, the x component, which is stretched, is larger than the y component, which is compressed. The skewness fluctuates around zero before the transition; it jumps to -0.4, which is reported as the value for isotropic turbulence.

The transition occurs after significant growth of enstrophy and the subsequent emergence of the inertial range (figure 14). The lower bound of the inertial range is defined as the wavenumber at which the timescale of the eddy becomes shorter than that of the base flow:

$$(k^2\varepsilon)^{-1/3} < \omega_0^{-1} \tag{3.5}$$

https://doi.org/10.1017/jfm.2014.439 Published online by Cambridge University Press

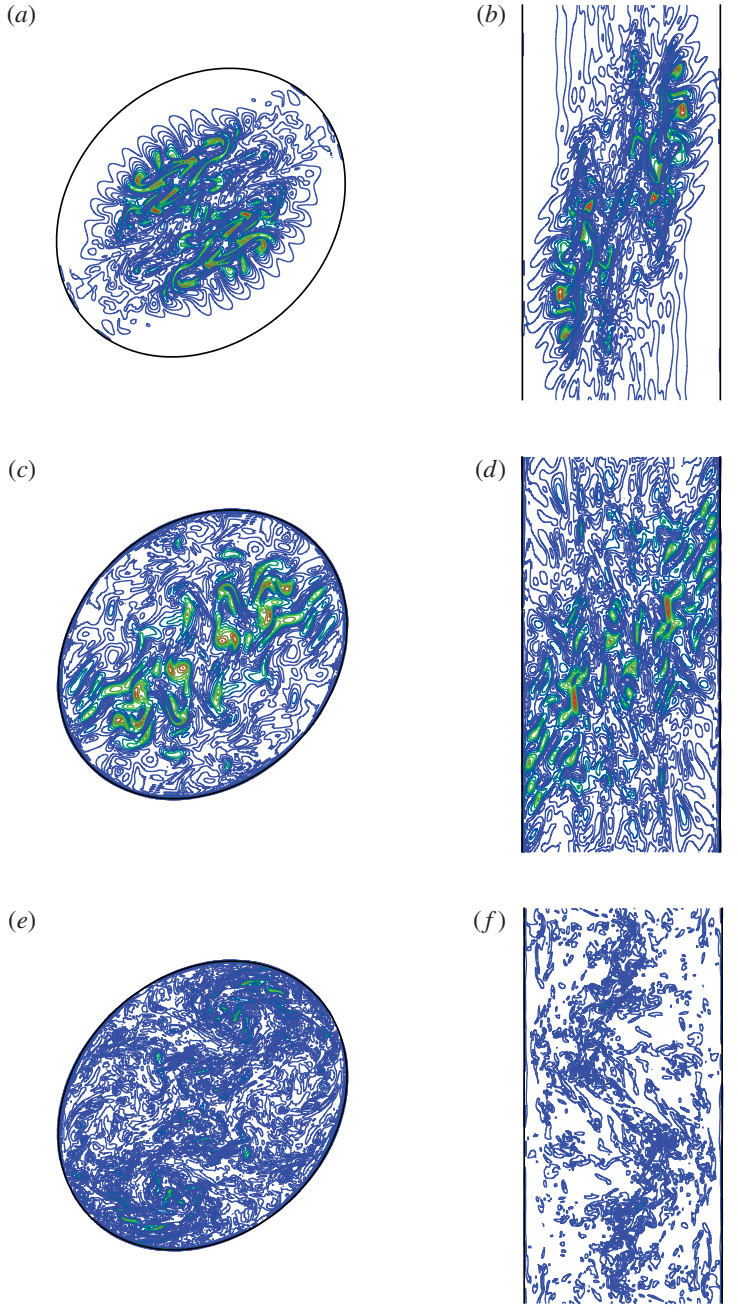


FIGURE 11. Structure of the disturbance in (*a*,*b*) the weakly nonlinear stage ($t = 100$), (*c*,*d*) the nonlinear stage ($t = 130$) and (*e*,*f*) the turbulent stage ($t = 180$). $\nu = 10^{-4}$. Contours of the magnitude of vorticity $|\boldsymbol{\omega}_d|$ on $z = 0$ (*a*,*c*,*e*) and $y = 0$ (*b*,*d*,*f*). The contour levels are the same as in figure 2.

https://doi.org/10.1017/jfm.2014.439 Published online by Cambridge University Press

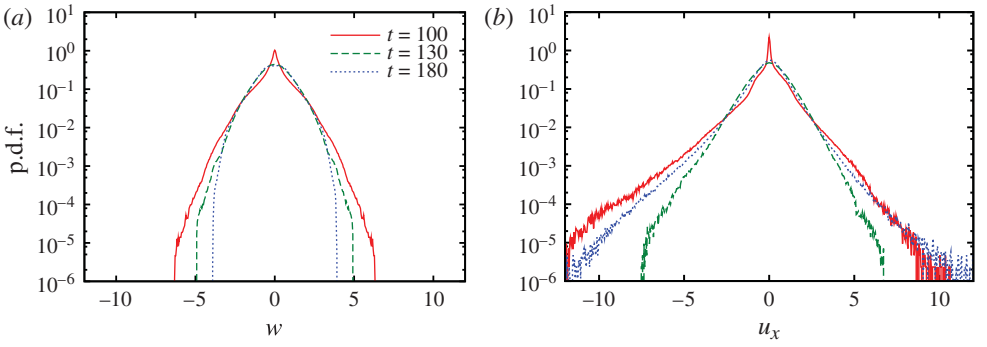


FIGURE 12. (Colour online) Normalized p.d.f. in the weakly nonlinear ($t = 100$), nonlinear ($t = 130$) and turbulent ($t = 180$) stages. $\nu = 10^{-4}$. (*a*) w, (*b*) $\partial u/\partial x$.

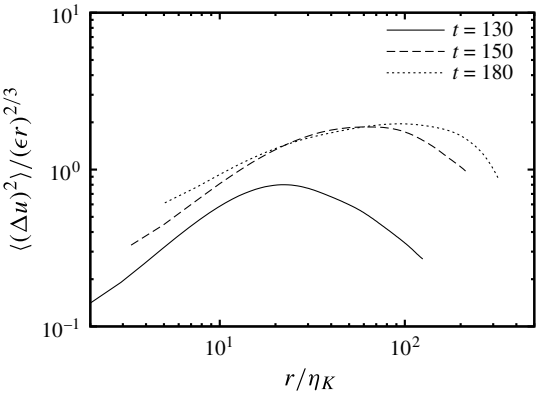


FIGURE 13. Second-order structure functions divided by $(\epsilon r)^{2/3}$ in the nonlinear ($t = 130$), transition ($t = 150$) and the turbulent stages ($t = 180$). $\nu = 10^{-4}$.

or $k > k_c = (\omega_0^3/\varepsilon)^{1/2}$, where ε is the dissipation rate of energy and $\omega_0 = 2$ is the uniform vorticity of the elliptical flow, since the process with the shorter timescale dominates the dynamics; a similar argument has explained successfully the transition of the energy spectrum in a shell model of rotating turbulence (Hattori, Ishizawa & Rubinstein 2004). The upper bound of the inertial range is defined as $k_d = 1/(10\eta_K)$ above which the energy spectrum of isotropic turbulence deviates from the Kolmogorov spectrum. There is no inertial range for $t < 140$ except a tiny range observed in $90 < t < 105$, since k_c is larger than k_d. As the enstrophy and thereby the dissipation rate increases, k_c decreases and $k_d \propto \eta_K^{-1} = (\varepsilon/\nu^3)^{1/4}$ increases so that a wide inertial range appears after $t \approx 160$.

Figure 16 shows how the period of time spent in each stage depends on the Reynolds number by comparing $\nu = 1.5 \times 10^{-4}$ and 10^{-4}; the time evolution of the energy of disturbance is shifted as $t = t + 26$ for $\nu = 10^{-4}$ for comparison. In the linear stage, starting from nearly the same value of energy, the period of time increases as the Reynolds number decreases since the growth rate is reduced by viscous effects. After the beginning of the weakly nonlinear stage, however, the time evolution of energy for $\nu = 1.5 \times 10^{-4}$ is similar to that for $\nu = 10^{-4}$. The time of transition to turbulence is also checked by the time evolution of the y component ratio of

https://doi.org/10.1017/jfm.2014.439 Published online by Cambridge University Press

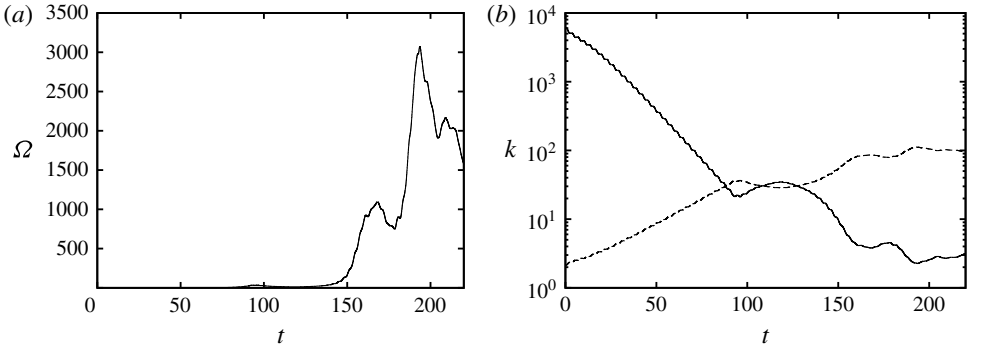


FIGURE 14. Time evolution of (*a*) enstrophy and (*b*) inertial range. The inertial range is defined as $k_c < k < k_d$, where $k_c = (\omega_0^3/\varepsilon)^{1/2}$ and $k_d = 1/(10\eta_K)$ are shown by the solid and dashed lines, respectively. $\nu = 10^{-4}$.

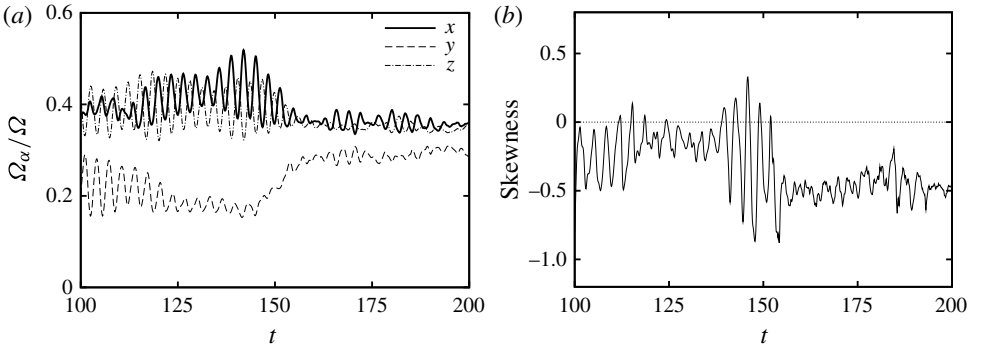


FIGURE 15. Time evolution of (*a*) the component ratio of enstrophy and (*b*) skewness of $\partial u/\partial x$. $\nu = 10^{-4}$.

enstrophy (figure 16*b*), which is shown to be a sign of the transition in figure 15. The time difference between the transitions of the two cases is $25 \sim 30$ which is close to the shift of time of 26 used in figure 16(*a*). Thus the period of time of each stage is nearly the same after the beginning of the weakly nonlinear stage as long as the initial disturbance is unchanged. This implies that nonlinear dynamics takes over the elliptic instability from the weakly nonlinear stage to the turbulent stage, although turbulence is weakly asymmetric because of strain.

3.6. *Turbulent stage*

Figures 10(*d*) and 17 confirm that the energy spectrum has an inertial range proportional to $k^{-5/3}$ for $t \geqslant 160$. The inertial range is rather narrow at $t = 160$ and 180 as the spectrum deviates from the Kolmogorov spectrum at low wavenumbers. It becomes wider at $t = 200$ and 220 in accordance with figure 14. The Kolmogorov constant estimated by flat regions in figure 17 is reasonably close to the value 1.62 ± 0.17 summarized by Sreenivasan (1995). Correspondingly, fine-scale structures develop in the vorticity field (figure 11*e*,*f*). The Reynolds number based on the Taylor microscale is $Re_\lambda = 261$ at $t = 180$. The p.d.f. of w is Gaussian, while that of $\partial u/\partial x$ shows strong intermittency, which is one of the important characteristic features

https://doi.org/10.1017/jfm.2014.439 Published online by Cambridge University Press

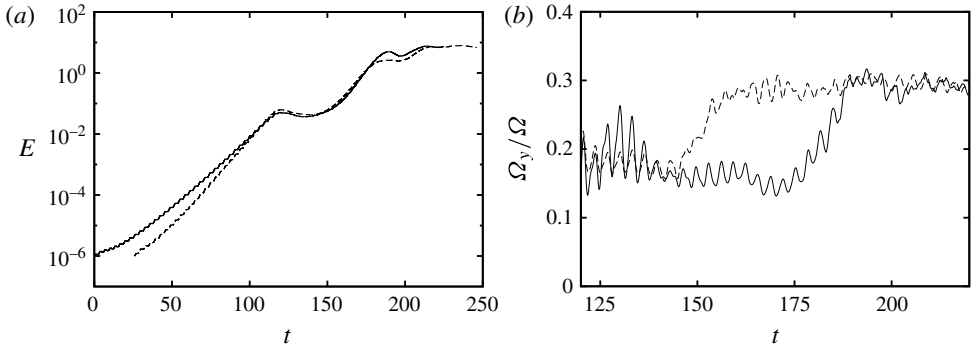


FIGURE 16. Comparison of time evolution for $\nu = 1.5 \times 10^{-4}$ (solid line) and 10^{-4} (dashed line): (*a*) energy of the disturbance (the result for $\nu = 10^{-4}$ is shifted as $t = t + 26$); (*b*) y component ratio of enstrophy.

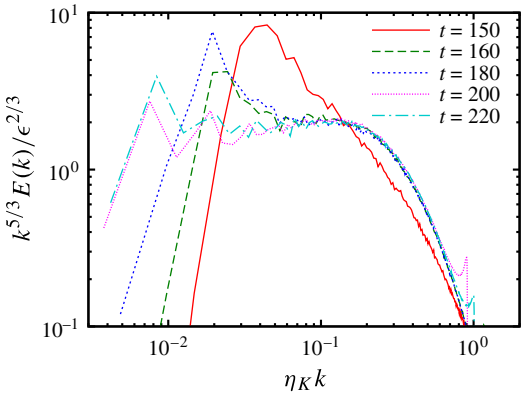


FIGURE 17. (Colour online) Compensated energy spectrum in the turbulent stage. $\nu = 10^{-4}$.

of isotropic turbulence; the probability of large magnitude of $\partial u/\partial x$ is larger than that in the weakly nonlinear stage. The second-order structure function has a range approximately proportional to $r^{2/3}$ at $t = 180$; the scaling exponent is slightly larger than 2/3, known as anomalous scaling (see e.g. Davidson 2004). The ratios of the energy and the enstrophy of the disturbance to the elliptical flow are approximately 0.1–0.2 and 0.8, respectively, implying that the base flow is still stronger than the disturbance. As a result there is asymmetry due to rotation and strain as shown in the previous subsection.

The effects of a developed disturbance on the mean flow are also investigated. Figure 18 compares the time evolution of energy of the mean flow, the disturbance and the total energy which coincides with the sum of the former two. The total energy is nearly constant until $t \approx 150$. Then in the turbulent stage the energy of the disturbance increases significantly, while the total energy as well as the energy of the mean flow decrease. Figure 19 shows that the ratio of the lost energy to the initial energy of the mean flow is large in the core region in the turbulent stage. In other words the mean flow approaches a hollow vortex, pushing vorticity outward. Although the energy of the mean flow is still decreasing at the final time of simulation, the rate

https://doi.org/10.1017/jfm.2014.439 Published online by Cambridge University Press

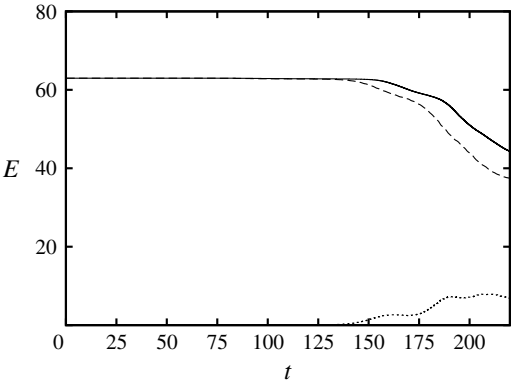


FIGURE 18. Time evolution of energy of the whole flow (solid line), mean flow (dashed line) and disturbance (dotted line). $\nu = 10^{-4}$.

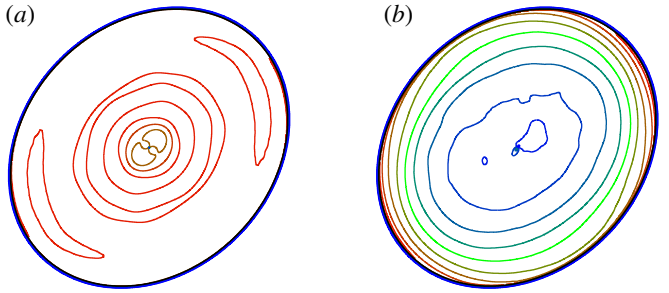


FIGURE 19. Energy ratio of mean flow to elliptical flow. The contours correspond to 10 % (blue line), 20 %, ..., and 100 % (red line). Average for (*a*) $107 \leqslant t \leqslant 113$ and (*b*) $207 \leqslant t \leqslant 213$.

of decrease is also decreasing and the energy of the disturbance reaches a constant with small fluctuation, suggesting that the flow is statistically steady.

4. Concluding remarks

We have investigated the time evolution of localized disturbances in elliptical flow by means of DNS. We have captured the unstable growth of localized disturbances predicted by the short-wavelength stability analysis. The time evolution is divided into four stages: the linear, weakly nonlinear, nonlinear and turbulent stages. In the linear stage a single wavepacket grows exponentially without changing its shape. The exponential growth is accompanied by large oscillations whose time period is a half of the rotation in the elliptical flow. An averaged wavepacket, which is a train of bending waves that has a finite spatial extent, also grows exponentially although the oscillations of the growth rate are small. The averaged growth rate increases as the kinematic viscosity decreases; the inviscid limit is close to the value predicted by the short-wavelength stability analysis.

In the weakly nonlinear stage the energy stops growing. The vortical structure of the initial disturbances is deformed into wavy patterns. The energy spectrum loses the peak at the initial wavenumber, developing a broad spectrum, and the flow goes into

https://doi.org/10.1017/jfm.2014.439 Published online by Cambridge University Press

the next stage. In the nonlinear stage although strong vorticity is still localized, weak vorticity is scattered in the whole domain. The p.d.f.s of w and $\partial u/\partial x$ are similar to those of isotropic turbulence; however, the energy spectrum does not have an inertial range showing a $k^{-5/3}$ spectrum. Transition to turbulence occurs within three rotations of the elliptical flow as mean values of the component ratio of enstrophy and the skewness change. Finally, in the turbulent stage fine-scale structures appear in the vorticity field. The p.d.f. of $\partial u/\partial x$ shows the strong intermittency known for isotropic turbulence. The energy spectrum attains an inertial range showing a $k^{-5/3}$ spectrum. The turbulence is not symmetric because of rotation and strain; the y component of vorticity, which is in the compressing direction, is smaller than the other two components. It should be noted that the whole process of a small localized disturbance leading to turbulence is elucidated; there are few numerical studies in this context, though Kerr (2013) has investigated the process by which a pair of vortex pairs perturbed locally develops into turbulence.

The present results suggest that introducing localized disturbances can be an effective way to destabilize vortical flows subjected to parametric instability. The viscous damping of the growth rate can be small, depending on the Reynolds number and the magnitude of wavenumber. For example, in the present case (3.4) predicts that the difference between the growth rate at $Re_\Gamma = 10^6$ and the inviscid limit is less than 5 % when $k_0 \leqslant 50$. As a result the growth rate of the localized disturbances can be comparable with that of the unstable normal modes of low wavenumber like the bending waves. Thus it would be possible to destabilize and destroy wingtip vortices behind aircraft whose Reynolds number is typically larger than 10^6 by introducing appropriate localized disturbances. Correspondingly, the inviscid growth rate of the first principal modes of the elliptic instability are nearly constant and close to the value in the short-wave limit (Eloy & Le Dizès 2001; Fukumoto 2003); a number of modes compete when the Reynolds number is large.

Some future works are suggested below. The time evolution of localized disturbances in other vortices is of interest since elliptical flow has two characteristic features that general vortices do not possess. One is that the elliptical flow is in the state of rigid-body rotation, while vortices are generally in differential rotation in the sense that the angular velocity depends on the radius. In such vortices the differential rotation or shear deform localized disturbances so that the stability properties can change significantly. If localized disturbances of high wavenumber and small spatial extent are introduced near the axis of vortices where they are almost in rigid-body rotation, the results would be similar to the present results. However, if the above conditions are not satisfied, the deformation due to shear may hinder the instability while the resonance condition for the direction of the wavenumber is changed (Hattori & Fukumoto 2003; Hattori & Hijiya 2010). The other feature is that there is an input of energy at the wall in the present elliptical flow, while no energy is input to vortices which are far from solid boundaries. In the present case when the flow reaches the turbulent stage the energy of the mean flow decreases significantly. What happens for vortices far from solid boundaries should be investigated in detail since it is a key process for destabilization of vortices; processes like the re-formation of elliptical vortices observed in Schaeffer & Le Dizès (2010) may occur.

The details of the transition from the nonlinear to the turbulent stage are also of much interest. Although we have explored some important features including the changes in the energy spectrum, the p.d.f. and the energy ratio, the mechanism by which fine-scale vortical structures are generated, for example, should be understood.

https://doi.org/10.1017/jfm.2014.439 Published online by Cambridge University Press

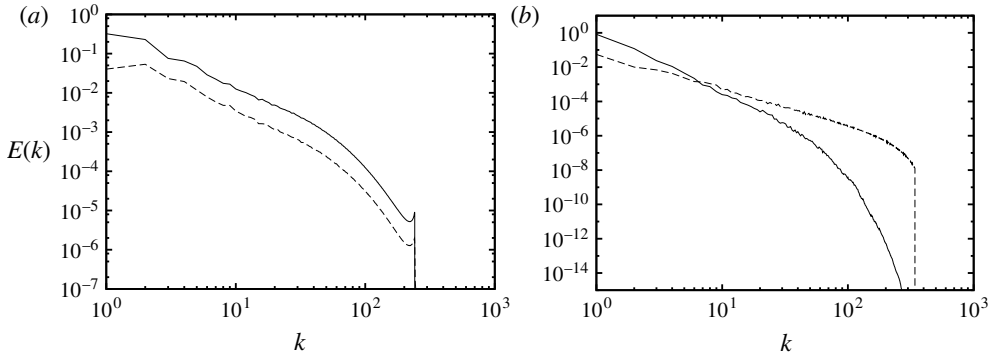


FIGURE 20. Effects of filtering on the energy spectrum of isotropic turbulence. The solid lines are the original spectrum, while the dashed lines are the filtered spectrum. (*a*) Three dimensions, (*b*) two dimensions.

Acknowledgements

This work was supported by JSPS KAKENHI 24540391. Numerical calculations were performed on the Altix UV1000 at the Institute of Fluid Science, Tohoku University.

Appendix A. Energy spectrum in the elliptical cylinder

We have employed the simple definition of the energy spectrum (2.12) although the fluid domain is restricted to an elliptic cylinder in a periodic box. As discussed in § 2.4 the jump at the boundary of the elliptic cylinder can make the energy spectrum spurious. To check the effects of the jump we apply a filter to the energy spectrum of two-dimensional and three-dimensional isotropic turbulence and find the difference between the original and filtered spectra.

The data of the three-dimensional isotropic turbulence are taken from those used in Hattori & Ishihara (2012); it is a forced turbulence and the number of modes is 512^3. The data of the two-dimensional isotropic turbulence are taken from Terakado & Hattori (2014); it is a decaying turbulence and the number of modes is 1024^2. The filtered data are obtained by multiplying the velocity field by $1 - \Xi$.

Figure 20 compares the original and filtered spectra. In three dimensions the two spectra, both of which have an inertial range $E(k) \propto k^{-5/3}$, are nearly parallel except near the lowest wavenumber, showing that filtering does not affect the nature of the energy spectrum. In two dimensions, on the other hand, the filtered spectrum has a range proportional to k^{-2}, while the inertial range of the original spectrum is proportional to k^{-3}; this is an artifact of filtering that creates severe jumps at the boundary. Therefore, a spectrum steeper than k^{-2} can be affected by filtering. However, we do not observe k^{-2} scaling in the energy spectrum in any stage (figure 10). This shows that the jumps at the boundary in the present case are not so severe as the field of homogeneous turbulence multiplied by the Heaviside function as a filter; before the turbulent stage the strong fluctuations due to the disturbance are localized and the velocity field decays smoothly at the surface of the cylinder. Therefore the effects of the jump at the boundary are negligible in the turbulent stage and not so severe in the other stages.

https://doi.org/10.1017/jfm.2014.439 Published online by Cambridge University Press

Appendix B. Check of numerical accuracy

Two tests are done in order to check numerical accuracy of the numerical simulations. First the linear growth rate of an unstable eigenmode of the elliptic instability is obtained using the same code as in the present study and compared to the value obtained by modal stability analysis. This problem has been studied by Mason & Kerswell (1999) and Eloy, Le Gal & Le Dizès (2003).

The mode we chose is a sum of stationary Kelvin waves whose azimuthal wavenumber is $m = \pm 1$ in the limit of small strain and viscosity; the Kelvin waves are given by

$$\boldsymbol{u}'_{\pm} = \hat{\boldsymbol{u}}_{\pm}(r)\mathrm{e}^{\mathrm{i}(\pm\theta+kz)}, \tag{B 1}$$

$$\hat{\boldsymbol{u}}_{\pm}(r) = \begin{bmatrix} \mp\mathrm{i}[\sqrt{3}kJ'_1(\sqrt{3}kr) + (2/r)J_1(\sqrt{3}kr)] \\ 2\sqrt{3}kJ'_1(\sqrt{3}kr) + (1/r)J_1(\sqrt{3}kr) \\ \mp 3kJ_1(\sqrt{3}kr) \end{bmatrix} \tag{B 2}$$

in the cylindrical coordinate system that shares the z axis with the present coordinate system. We choose the first principal mode denoted by $(-1, 1, 1)$ in Eloy *et al.* (2003), for which $k = 1.5788$. This mode is not an exact eigenmode in the elliptical cylinder; in addition it does not satisfy no-slip boundary conditions at the surface of the cylinder. Thus before performing the simulation using the present code we developed a code that solves the linearized version of (2.9) and performed a long calculation starting from the above mode; the outcome is close to the most unstable eigenmode since the other modes grow slower than it or decay; no-slip boundary conditions are satisfied thanks to the penalization terms. Then it is rescaled and used as an initial condition of (2.9).

The growth rate of the above mode in the inviscid limit has been obtained by modal stability analysis: $\sigma_{inv} = 0.5312$ (Eloy *et al.* 2003). A viscous correction should be taken into account, though. We follow Eloy *et al.* (2003) in which two viscous terms are introduced in the amplitude equation:

$$\frac{\mathrm{d}A_{\pm}}{\mathrm{d}t} = \epsilon\sigma_{inv}A_{\mp} - Re^{-1/2}sA_{\pm} - Re^{-1}vA_{\pm}, \tag{B 3}$$

where $A_{\pm}$ is the amplitude of the Kelvin waves and s and v are constants; the terms $Re^{-1/2}sA_{\pm}$ and $Re^{-1}vA_{\pm}$ are due to viscous damping in the boundary layer and the bulk, respectively. The growth rate reads

$$\sigma = \epsilon\sigma_{inv} - Re^{-1/2}s - Re^{-1}v. \tag{B 4}$$

The value of s can be obtained from the fact that the critical Reynolds number is $Re_c = 435$ when $\epsilon = 0.1 = \epsilon_1$:

$$0 = \epsilon_1\sigma_{inv} - Re_c^{-1/2}s - Re_c^{-1}v. \tag{B 5}$$

Eliminating s in (B 4) using (B 5) we obtain

$$\sigma = \epsilon\sigma_{inv}\left[1 - \frac{\epsilon_1}{\epsilon}\left(\frac{Re_c}{Re}\right)^{1/2}\right] + (Re^{-1/2}Re_c^{-1/2} - Re^{-1})v. \tag{B 6}$$

The value of v is approximated by the square of the magnitude of the wavevector whose radial component is approximated by $\sqrt{3}k$: $v = (3k^2 + k^2)/R^2 = 4k^2/R^2$. The

https://doi.org/10.1017/jfm.2014.439 Published online by Cambridge University Press

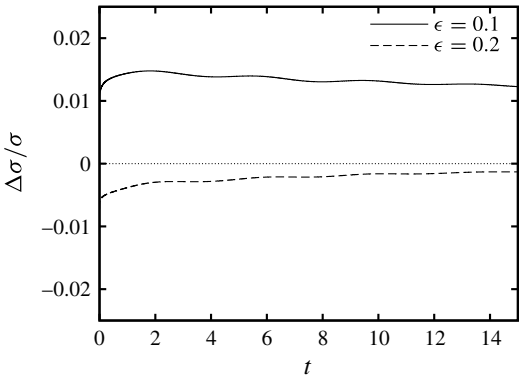


FIGURE 21. Relative error of instantaneous growth rate obtained by DNS. $\nu = 10^{-4}$.

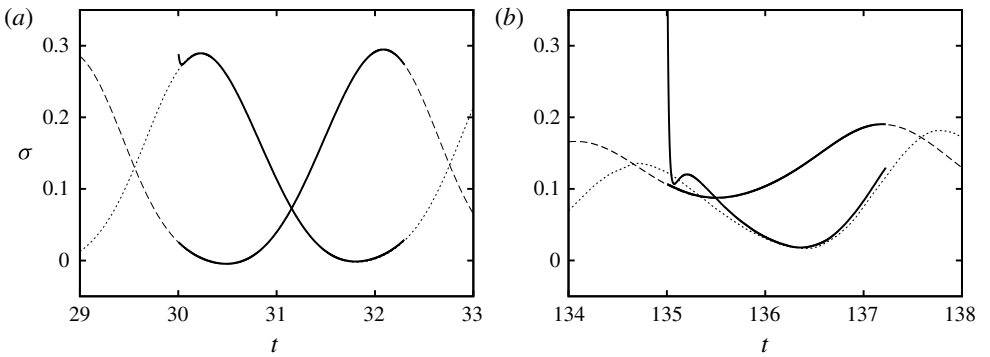


FIGURE 22. Comparison of instantaneous growth rate obtained by different resolutions. The dashed and dotted lines are the growth rates of energy and enstrophy of the disturbance obtained using 512^3 modes. The thick solid lines are those obtained using 1024^3 modes. $\nu = 10^{-4}$. (*a*) Linear stage, (*b*) nonlinear stage.

resulting values of the growth rate are $\sigma = 0.0471$ and 0.1003 for $\epsilon = 0.1$ and 0.2, respectively, when $Re = 2.4674 \times 10^4$ or $\nu = 10^{-4}$.

The numerical results are shown in figure 21. The relative error is defined as the difference between the instantaneous growth rate and (B 6) divided by the latter. After a short initial transient the error approaches a small constant: $\Delta\sigma/\sigma \approx 1.2\,\%$ and $-0.2\,\%$ for $\epsilon = 0.1$ and $\epsilon = 0.2$, respectively. These values are reasonably small as the analytical values are approximate ones obtained in the limit of small strain.

Next calculations with higher resolution were performed and compared to the present results. The number of modes was increased to 1024^3 and the calculations started from $t = 30$ (linear stage) and $t = 135$ (nonlinear stage) using the stored data. Figure 22 compares the time evolution of the instantaneous growth rate of energy and enstrophy of the disturbance. The growth rate of energy does not change with increasing resolution as the two cases coincide not only in the linear stage but also in the nonlinear stage. A small initial transient is observed in the growth rate of enstrophy in the linear stage; apart from that the two cases coincide. The initial

https://doi.org/10.1017/jfm.2014.439 Published online by Cambridge University Press

transient is large in the nonlinear stage because the enstrophy spectrum extends to high wavenumbers; after the transient, however, the difference between the two cases is small.

The results of the two tests confirm that our numerical results are sufficiently accurate.

REFERENCES

ANGOT, P., BRUNEAU, C.-H. & FABRIE, P. 1999 A penalization method to take into account obstacles in incompressible viscous flows. *Numer. Math.* **81**, 497–520.

ARENDT, S., FRITTS, D. C. & ANDREASSEN, Ø. 1997 The initial value problem for Kelvin vortex waves. *J. Fluid Mech.* **344**, 181–212.

ARQUIS, E. & CALTAGIRONE, J. P. 1984 On the hydrodynamical boundary-conditions along a fluid layer porous-medium interface – application to the case of free-convection. *C. R. Acad. Sci. Paris* II **299**, 1–4.

BAYLY, B. J. 1986 Three-dimensional instability of elliptical flow. *Phys. Rev. Lett.* **57**, 2160–2163.

COHEN, J., SHUKHMAN, I. G., KARP, M. & PHILIP, J. 2010 An analytical-based method for studying the nonlinear evolution of localized vortices in planar homogeneous shear flows. *J. Comput. Phys.* **229**, 7765–7773.

CROW, S. C. 1970 Stability theory for a pair of trailing vortices. *AIAA J.* **8**, 2172–2179.

DAVIDSON, P. A. 2004 *Turbulence – An Introduction for Scientists and Engineers*. Oxford University Press.

ELOY, C. & LE DIZÈS, S. 2001 Stability of the Rankine vortex in a multipolar strain field. *Phys. Fluids* **13**, 660–676.

ELOY, C., LE GAL, P. & LE DIZÈS, S. 2000 Experimental study of the multipolar vortex instability. *Phys. Rev. Lett.* **85**, 3400–3403.

ELOY, C., LE GAL, P. & LE DIZÈS, S. 2003 Elliptic and triangular instabilities in rotating cylinders. *J. Fluid Mech.* **476**, 357–388.

FADDY, J. M. & PULLIN, D. I. 2005 Flow structure in a model of aircraft trailing vortices. *Phys. Fluids* **17**, 085106.

FRIEDLANDER, S. & VISHIK, M. M. 1991 Instability criteria for the flow of an inviscid incompressible fluid. *Phys. Rev. Lett.* **66**, 2204–2206.

FUKUMOTO, Y. 2003 The three-dimensional instability of a strained vortex tube revisited. *J. Fluid Mech.* **493**, 287–318.

FUKUMOTO, Y. & HATTORI, Y. 2005 Curvature instability of a vortex ring. *J. Fluid Mech.* **526**, 77–115.

GLEDZER, E. B. & PONOMAREV, V. M. 1992 Instability of bounded flows with elliptical streamlines. *J. Fluid Mech.* **240**, 1–30.

GODEFERD, F. S., CAMBON, C. & LEBLANC, S. 2001 Zonal approach to centrifugal, elliptic and hyperbolic instabilities in Stuart vortices with external rotation. *J. Fluid Mech.* **449**, 1–37.

HATTORI, Y. & FUKUMOTO, Y. 2003 Short-wavelength stability analysis of thin vortex rings. *Phys. Fluids* **15**, 3151–3163.

HATTORI, Y. & FUKUMOTO, Y. 2009 Short-wavelength stability analysis of a helical vortex tube. *Phys. Fluids* **21**, 014104.

HATTORI, Y. & FUKUMOTO, Y. 2010 Short-wave stability of a helical vortex tube: the effect of torsion on the curvature instability. *Theor. Comput. Fluid Dyn.* **24**, 363–368.

HATTORI, Y. & FUKUMOTO, Y. 2012 Effects of axial flow on the stability of a helical vortex tube. *Phys. Fluids* **24**, 054102.

HATTORI, Y. & FUKUMOTO, Y. 2014 Modal stability analysis of a helical vortex tube with axial flow. *J. Fluid Mech.* **738**, 222–249.

HATTORI, Y. & HIJIYA, K. 2010 Short-wavelength stability analysis of Hill's vortex with/without swirl. *Phys. Fluids* **22**, 074104.

https://doi.org/10.1017/jfm.2014.439 Published online by Cambridge University Press

HATTORI, Y. & ISHIHARA, T. 2012 4D visualization of isotropic turbulence and dynamics of high-enstrophy structures. In *Proceedings JSST 2012 (International Conference on Simulation Technology)*, pp. 170–174.

HATTORI, Y., ISHIZAWA, A. & RUBINSTEIN, R. 2004 Shell model for rotating turbulence. *Phys. Rev.* E **70**, 046311.

ISHIHARA, T., KANEDA, Y., YOKOKAWA, M., ITAKURA, K. & UNO, A. 2007 Small-scale statistics in high-resolution direct numerical simulation of turbulence: Reynolds number dependence of one-point velocity gradient statistics. *J. Fluid Mech.* **592**, 335–366.

KERR, R. 2013 Swirling, turbulent vortex rings formed from a chain reaction of reconnection events. *Phys. Fluids* **25**, 065101.

KERSWELL, R. R. 2002 Elliptical instability. *Annu. Rev. Fluid Mech.* **34**, 83–113.

LANDMAN, M. J. & SAFFMAN, P. G. 1987 The 3-dimensional instability of strained vortices in a viscous-fluid. *Phys. Fluids* **30**, 2339–2342.

LAPORTE, F. & CORJON, A. 2000 Direct numerical simulations of the elliptic instability of a vortex pair. *Phys. Fluids* **12**, 1016–1031.

LE DIZÈS, S. & ELOY, C. 1999 Short-wavelength instability of a vortex in a multipolar strain field. *Phys. Fluids* **11**, 500–502.

LE DIZÈS, S. & LAPORTE, F. 2002 Theoretical predictions for the elliptical instability in a two-vortex flow. *J. Fluid Mech.* **396**, 73–108.

LEWEKE, T. & WILLIAMSON, C. H. K. 1998 Cooperative elliptic instability of a vortex pair. *J. Fluid Mech.* **360**, 85–119.

LIFSCHITZ, A. & HAMEIRI, E. 1991 Local stability conditions in fluid dynamics. *Phys. Fluids* A **3**, 2644–2651.

LUNDGREN, T. S. & MANSOUR, N. N. 1996 Transition to turbulence in an elliptic vortex. *J. Fluid Mech.* **307**, 43–62.

MALKUS, W. V. R. 1989 An experimental study of the global instabilities due to the tidal (elliptical) distortion of a rotating elastic cylinder. *Geophys. Astrophys. Fluid Dyn.* **48**, 123–134.

MASON, D. M. & KERSWELL, R. R. 1999 Nonlinear evolution of the elliptical instability: an example of inertial wave breakdown. *J. Fluid Mech.* **396**, 73–108.

MEUNIER, P. & LEWEKE, T. 2005 Elliptic instability of a co-rotating vortex pair. *J. Fluid Mech.* **533**, 125–159.

MOFFATT, H. K. 1967 The interaction of turbulence with strong wind shear. In *Proceedings of the International Colloquium on Atmospheric Turbulence and Radio Wave Propagation* (ed. A. M. Yaglom & V. I. Tatarski), pp. 139–156. Nauka.

MOORE, D. W. & SAFFMAN, P. G. 1975 The instability of a straight vortex filament in a strain field. *Proc. R. Soc. Lond.* A **346**, 413–425.

PIERREHUMBERT, R. T. 1986 Universal short-wave instability of two-dimensional eddies in an inviscid fluid. *Phys. Rev. Lett.* **57**, 2157–2159.

SCHAEFFER, N. & LE DIZÈS, S. 2010 Nonlinear dynamics of the elliptic instability. *J. Fluid Mech.* **646**, 471–480.

SCHNEIDER, K. & FARGE, M. 2005 Decaying two-dimensional turbulence in a circular container. *Phys. Rev. Lett.* **95**, 244502.

SHUKHMAN, I. G. 2007 Evolution of a localized vortex in plane nonparallel viscous flows with constant velocity shear. II. Elliptic flow. *Phys. Fluids* **19**, 017106.

SREENIVASAN, K. R. 1995 On the universality of the Kolmogorov constant. *Phys. Fluids* **7**, 2778–2784.

TERAKADO, D. & HATTORI, Y. 2014 Density distribution in two-dimensional weakly compressible turbulence. *Phys. Fluids* **26**, 085105.

TSAI, C.-Y. & WIDNALL, S. E. 1976 The stability of short waves on a straight vortex filament in a weak externally imposed strain field. *J. Fluid Mech.* **73**, 721–733.

WALEFFE, F. A. 1989 The 3D instability of a strained vortex and its relation to turbulence. PhD thesis, Massachusetts Institute of Technology.

WALEFFE, F. 1990 On the three-dimensional instability of strained vortices. *Phys. Fluids* A **2**, 76–80.

https://doi.org/10.1017/jfm.2014.439 Published online by Cambridge University Press